Precisely Gradient S-Doping to Optimize Oxysulfide Nanowires Active Centers for High-Rate Electrochemical Energy Storage

*Qingjun Yang[1], Xin Yin[1], Cuiqin Fang[1], Xinlong Liu[1], Yujue Yang[1], Jing Han[1], Yuejiao Chen[2], Bingang Xu[1]**

[1]Nanotechnology Center, Research Institute for Intelligent Wearable Systems, The Hong Kong Polytechnic University, Hung Hom, Kowloon, Hong Kong 999077, P.R. China
[2]State Key Laboratory for Powder Metallurgy, Central South University, Changsha, 410083, China
* Corresponding author, E-mail: tcxubg@polyu.edu.hk (B. Xu)

Keywords: Gradient S-doping, Core-shell nanowire, NiCo-O-S, GGA+U method, High capacitance

ABSTRACT: Owing to the high theoretical capacitance, Nickel cobalt alkaline carbonate (NiCo-AC) has attracted wide attention in electrochemical energy storage. However, the high surface ionic resistance and low bulk intrinsic activity result in NiCo-AC being unable to exhibit fast electronic response frequency and charge storage. Herein, via precisely controlling gradient S-doping, NiCo-AC nanowire is in-situ converted into core-shell bimetallic oxysulfide (NiCo-O-S), with the interior particularly presenting granular state due to the contraction of bulk structure, achieving the synergistic modification of both surface and bulk. Specifically, owing to the lower band gap energy of metal sulfides, the derived shell effectively optimizes the OH^- adsorption center from Ni site to Ni-Co-Ni site with higher binding energy, and the granular core facilitates further ion diffusion with enhanced charge accumulation. Hence, NiCo-O-S nanoarrays reflect higher redox activity than that of NiCo-S and NiCo-AC, with an ultrahigh capacitance of 3,298 F g^{-1} at 1 A g^{-1}. The as-fabricated supercapacitors display an outstanding energy density of 131 Wh kg^{-1} at 800 W kg^{-1} and present a high capacitance retention of 98.5% and coulomb efficiency of 93.2% under 12,000 charge-discharge cycles. This study reflects a new insight for activating the intrinsic activity of nanomaterials to further develop high-rate and stable electrodes.

1. Introduction

Supercapacitors have emerged as pivotal electrochemical energy storage equipment because of high-power density, rapid charge-discharge capabilities, and long lifespan [1-4]. The quest for advanced electrode materials that can deliver high capacitance while maintaining the intrinsic fast charge-discharge characteristics is at the forefront of supercapacitor research [5, 6]. Owing to the easily tunable nanostructure and high theoretical capacitance, nickel cobalt alkaline carbonate (NiCo-AC) has

attracted considerable attention as potential electrode materials [7, 8]. Recent studies have primarily concentrated on the synthesis and application of NiCo-AC in supercapacitors, revealing promising electrochemical performance [9, 10]. Nevertheless, the relatively low intrinsic activity leads to slower redox kinetics, which is the critical challenges that limit the electrochemical energy storage efficiency [11]. Another main reason is the low bulk electronic conductivity and high surface ionic resistance, which leads to high impedance, slow response frequency and large capacitance loss [12].

To break through these bottlenecks, considerable efforts have been made to tap into the energy storage potential of NiCo-AC. For instance, designing nanoarray electrode materials with different dimensions, including 1D nanowires and 2D nanosheets, has demonstrated good dispersibility and structural stability [13, 14]. In particular, NiCo-AC nanowire arrays have shown very promising tunability, such as composite structural design [15], metal ion ratio regulation [16], defect structure engineering [17], and anion doping [18]. Significantly, anion doping can better in-situ modulate the redox reaction activity and the electronic structural state, thereby promoting NiCo-AC nanowire arrays to exhibit higher conductivity, capacitance, and structural stability [19, 20]. However, the refined anion regulation to explore changes in active sites and energy storage characteristics has not been implemented despite the urgent need.

Herein, precisely gradient sulfidation has been proposed as an effective strategy to enhance the capacitance and conductivity of NiCo-AC nanowire. By finely controlling the concentration and duration of hydrothermal sulfidation, sulfur ions replaced partial oxygen atoms to varying extents, causing the nanowire to gradually contract internally and transform in-situ into nanoparticles, ultimately constructing core-shell NiCo-O-S nanowire arrays. The unique graded structured electrode exhibits an ultrahigh capacitance of 3,298 F g^{-1} and 1,290 F g^{-1} at current density of 1 A g^{-1} and 50 A g^{-1}, respectively. The corresponding supercapacitors reflect outstanding energy density of 131 Wh kg^{-1} at the power density of 800 W kg^{-1}, excellent capacitance retention of 98.5%, and high coulomb efficiency of 93.2％ under 12,000 charge-discharge cycles. The outstanding charge storage capability is primarily attributed to this precisely collaborative regulation of surface and bulk. Firstly, the controllable gradient S-doping effectively regulates the intrinsic activity because of the lower band gap energy of metal sulfides, enhancing the kinetics of redox reactions. Then, the design of core-shell structure enhances the surface OH^- adsorption pathway, and the dispersed nanoparticles within the shell exhibit a higher active area to promote charge transfer and storage efficiency. Furthermore, the

gradient introduction of sulfur can create a compositional heterogeneity with rich variety of oxidation states from surface to bulk, potentially leading to a synergistic effect that enhances the activity and conductivity. Therefore, by elucidating the evolution process and mechanism of gradient vulcanization, theoretical support is provided for the exploration of high-performance electrode materials.

2. Results and discussion

2.1. Morphology and Structure

The evolution pathway of gradient sulfurization was demonstrated using crystal structures in **Figure 1**a. Specifically, we analyzed the structural characteristics of the (111) crystal plane during the gradient sulfurization process by cutting through the bulk structure. NiCo-AC exhibits a uniform and stable nanowire in-situ grown on carbon fibers without carrying any impurities (**Figure S1**), and the corresponding energy dispersive X-ray spectroscopy (EDS) reflects that NiCo-AC is composed of Co, Ni and O elements (**Figure S2**), which can provide a stable carrier for the gradient S-doping. According to XRD patterns (**Figure 1**b, c), there are obvious characteristic peaks of metal oxides (NiO_2 and Co_3O_4) and metal sulfides (Ni_3S_2, Co_9S_8 and $CoNi_2S_4$) when the concentration of sodium sulfide is 30 mM. The corresponding EDS proves the electrode material contains Ni, Co, O, and S (**Figure S3**), indicating that S has replaced some of the O atoms (NiCo-O-S). In **Figure S4**, with the increase in sulfidation concentration, NiCo-AC completely transforms into NiCo-S. X-ray photoelectron spectroscopy (XPS) spectra of NiCo-AC, NiCo-O-S and NiCo-S are compared and analyzed. In **Figure 1**d, Ni $2p_{3/2}$ at 858.3 eV, 857.2 eV and Ni $2p_{1/2}$ at 857.5 eV, 873.8 eV reflect the existence of Ni^{2+} and Ni^{3+}. Meanwhile, the distinct characteristic peaks at 865.2 eV demonstrate the formation of Ni-O-S. In **Figure 1**e, these peaks located at 781.9 eV and 800.6 eV indicate Co have two valence states, including Co^{2+} and Co^{3+}, which is consistent with peaks at 798.4 eV and 784.5 eV. Significantly, the peak at 782.9 eV proves the existence of Co-O-S. Therefore, precise regulation of hydrothermal vulcanization can induce in-situ conversion of NiCo-AC to NiCo-O-S. As shown in **Figure 1**f, partial O atoms are replaced by S atoms, leading to a rise of O binding energy and the transformation of metal oxides (O_m) into defective oxygen (O_v) and adsorbed oxygen (O_{ads}). As NiCo-AC is completely transformed into NiCo-S, the O_m gradually disappears. Additionally, the XPS spectra of S indicates the M-O-S characteristic peak, reflecting the formation of NiCo-O-S (**Figure 1**g).

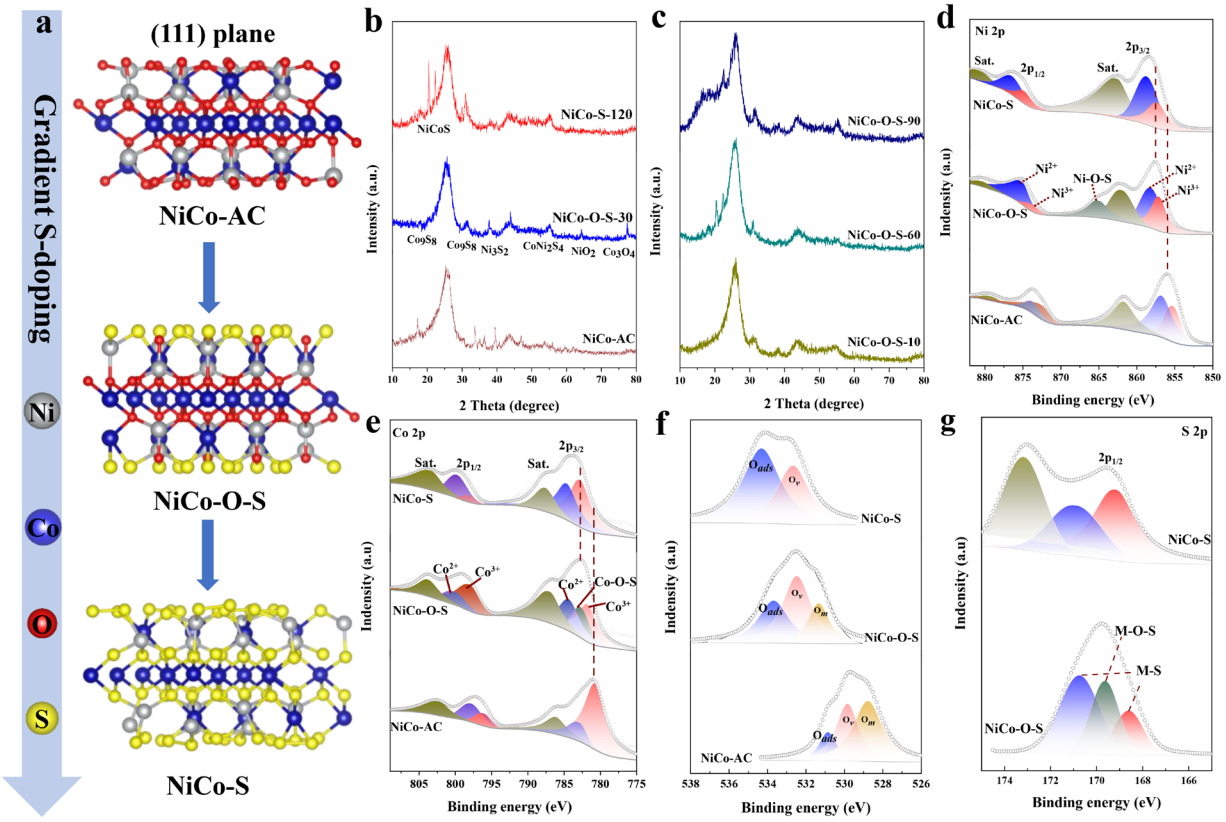

Figure 1. a) Schematic of the evolution process based on atomic configurations. b) XRD patterns of NiCo-AC, NiCo-O-S in 30 mM sulfurization concentration and NiCo-S in 120 mM sulfurization concentration. c) XRD patterns of NiCo-O-S in different sulfurization concentration (10, 60, 90). d) Ni 2p, e) Co 2p and f) O 1s orbital XPS spectra of NiCo-AC, NiCo-O-S and NiCo-S. g) S 2p orbital XPS spectras of NiCo-AC, NiCo-O-S and NiCo-S.

According to transmission electron microscopy (TEM) images, the evolution process of gradient sulfidation of NiCo-AC is accurately analyzed. By regulating the concentration of the reaction substrate, we found that the core-shell structure gradually emerged (**Figure 2**a, b). As the concentration of sodium sulfide was 30 mM, the stable shell with a thickness of 13.5 nm was formed, reflecting the successful preparation of the core-shell NiCo-O-S nanowire (**Figure 2**c). Significantly, the internal structure of the nanowire exhibits a granular state. As the concentration increases, the core-shell structure is gradually destroyed (**Figure 2**d, e). When the concentration of sodium sulfide increases to 120mM (**Figure 2**f), the nanowire is broken and completely transform into bimetallic sulfides (NiCo-S). The SEM images with different sulfide concentrations show that the structure of nanowires is completely destroyed at a sodium sulfide concentration of 150 mM (**Figure S5**). As shown in **Figure 2**g, the original NiCo-AC nanowire shell thickness is 8 nm. We further investigated the impact of time gradient on core-shell structure when sodium sulfide was 30mM. As the vulcanization time prolongs,

the shell begins to disappear and gradually presents a clear core-shell structure (**Figure 2**h, i). At 2.5 h, a stable shell with a thickness of 13.2 nm was formed (**Figure 2**j). At time gradients of 3.5 h and 4.5 h, the shell disappears and the nanowires exhibit complete granulation (**Figure 2**k, l). By precisely controlling the concentration gradient and time gradient, we have described in detail the evolution process of core-shell nanowires with internal granular structures, which provides a significant reference for the gradient modification research of nanomaterials.

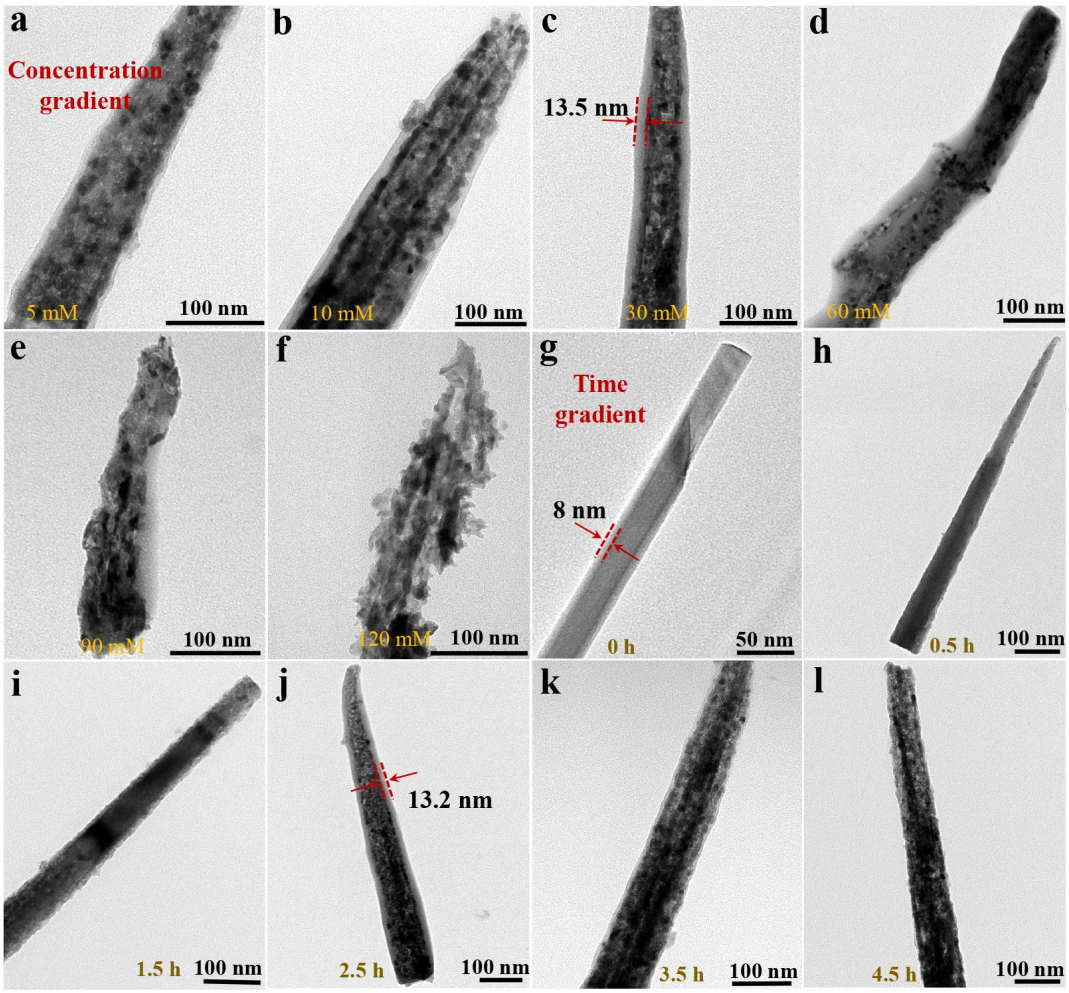

Figure 2. The TEM images NiCo-O-S with gradient S-doping via sodium sulfide of different concentrations a) 5 mM, b) 10 mM, c) 30 mM, d) 60 mM, e) 90 mM and f) 120 mM. The TEM images of NiCo-O-S with gradient S-doping via sodium sulfide of different time g) 0 h, h) 0.5 h, i) 1.5 h, j) 2.5 h, k) 3.5 h and l) 4.5 h.

According to the high-resolution TEM (HRTEM) image (**Figure 3**a), the lattice spacing of 1.2 Å reflects the (622) crystal plane of NiCo-AC is predominantly composed of $CoNi_2O_4$, and the shell part does not exhibit distinct lattice features. In **Figure 3**b, the lattice spacing of 5.3 Å, 3.4 Å and 2.8 Å represent the (111) crystal plane of $CoNi_2S_4$, (031) crystal plane of Ni-O-S and (220) crystal plane of NiCo-O-S based on the selected-area fast Fourier transform (FFT) patterns of the dark and light regions. Obviously, distinctive boundary can be clearly observed, with well-defined nanoparticles in the core

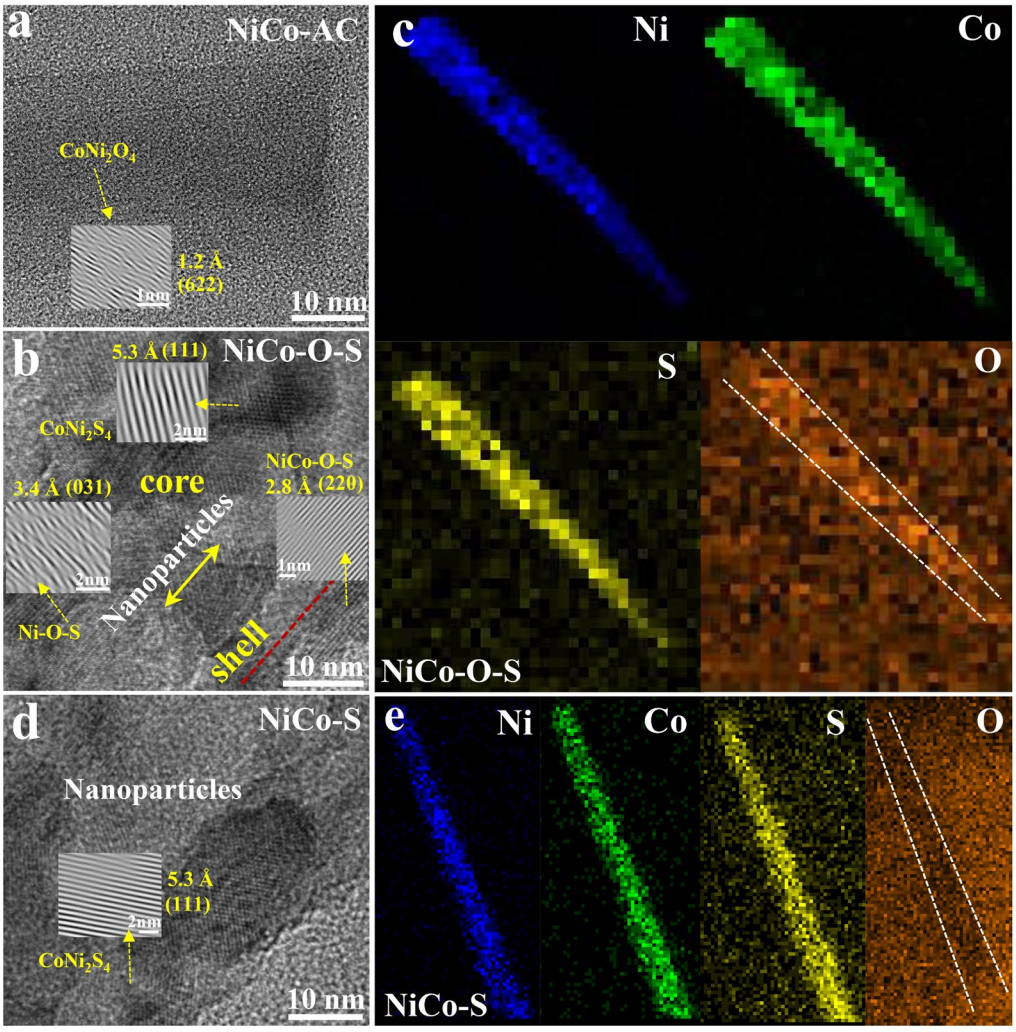

Figure 3. The HRTEM images of a) NiCo-AC and b) NiCo-O-S with corresponding FFT patterns. c) The element mapping images of NiCo-O-S. d) The HRTEM image of NiCo-S with corresponding FFT patterns. e) The element mapping images of NiCo-S.

and a single lattice orientation in the outer shell, fully showing the structural characteristics of NiCo-O-S. Moreover, the corresponding elemental mapping includes Ni, Co, O and S (**Figure 3**c), proving that the S partially replaces the O and S element is uniformly distributed throughout the single nanowire, while the distribution of O becomes blurred. Obviously, as the sulfide gradient deepens, the nanowire is completely in a granular state, and the core-shell structure has disappeared. The lattice spacing of 5.3 Å represents the (111) crystal plane of $CoNi_2S_4$ (**Figure 3**d), reflecting the characteristics of NiCo-S. As described in **Figure 3**e, for a single nanowire, the elements Ni, Co, and O can be clearly observed, while the O element has completely disappeared. This demonstrates that S atoms have entirely replaced O atoms and confirms the formation of the bimetallic sulfide. Furthermore, since the sulfidation has not occurred, the entire nanowire of NiCo-AC does not reflect the composition of S

(Figure S6). The possible mechanism for the formation of core-shell structure is as follows. With the intensification of gradient sulfurization, the amorphous shell transforms into a crystalline bimetallic oxysulfide. The crystalline core, due to initial dissolution and subsequent recrystallization, forms the granular bimetallic oxysulfide, leading to a contraction in core volume and an increase in shell thickness from the original 8 nm to 13 nm.

2.2. Electrochemical Performance

A series of Cyclic Voltammetry (CV) and Galvanostatic Charge-Discharge (GCD) curves are employed to describe the charge storage of NiCo-AC, NiCo-S and NiCo-O-S. According to Figures S7 and S8, NiCo-O-S exhibits the largest CV closure curve area and longest discharge time at a sodium sulfide concentration of 30mM. In addition, the optimal time gradient and temperature conditions are determined by precisely adjusting the reaction time and temperature (Figures S9 and S10). Therefore, the optimal gradient conditions for the preparation of high-capacitance core-shell nanowires have been determined (30mM, 2.5h and 120℃). As shown in **Figure 4**a-c, the optimal mass capacitance (C_a) of the as-prepared NiCo-O-S nanowire arrays is up to 3,298 F g^{-1} at 1 A g^{-1}, which is higher than NiCo-AC (181.8 F g^{-1}) and NiCo-S (1,918 F g^{-1}) based on the formula 1. Furthermore, according to the energy dispersive X-ray spectroscopy based on SEM (SEM-EDS), we analyzed the mass percentage of elements in NiCo-O-S prepared with different sulfuration concentrations (0 mM, 5 mM, 10 mM, 30 mM, 60 mM, 90 mM and 120 mM) at the sulfuration time of 2.5 h (Table S1). As the sulfuration gradient increases, the mass content of O in NiCo-O-S significantly decreases while the content of S obviously increases. When NiCo-O-S reaches the optimal performance, the mass contents of each element are Ni-13.5%, Co-9.9%, O-58.5%, and S-18.1%, respectively.

$$C_a = i\Delta_t 10^{-3}/\Delta_V \Delta_{\mathrm{m}} \qquad (1)$$

Here i-current (mA), Δ_t-discharge time (s), Δ_V-voltage window (v), Δ_s-mass loading (2.0 mg cm^{-2}).

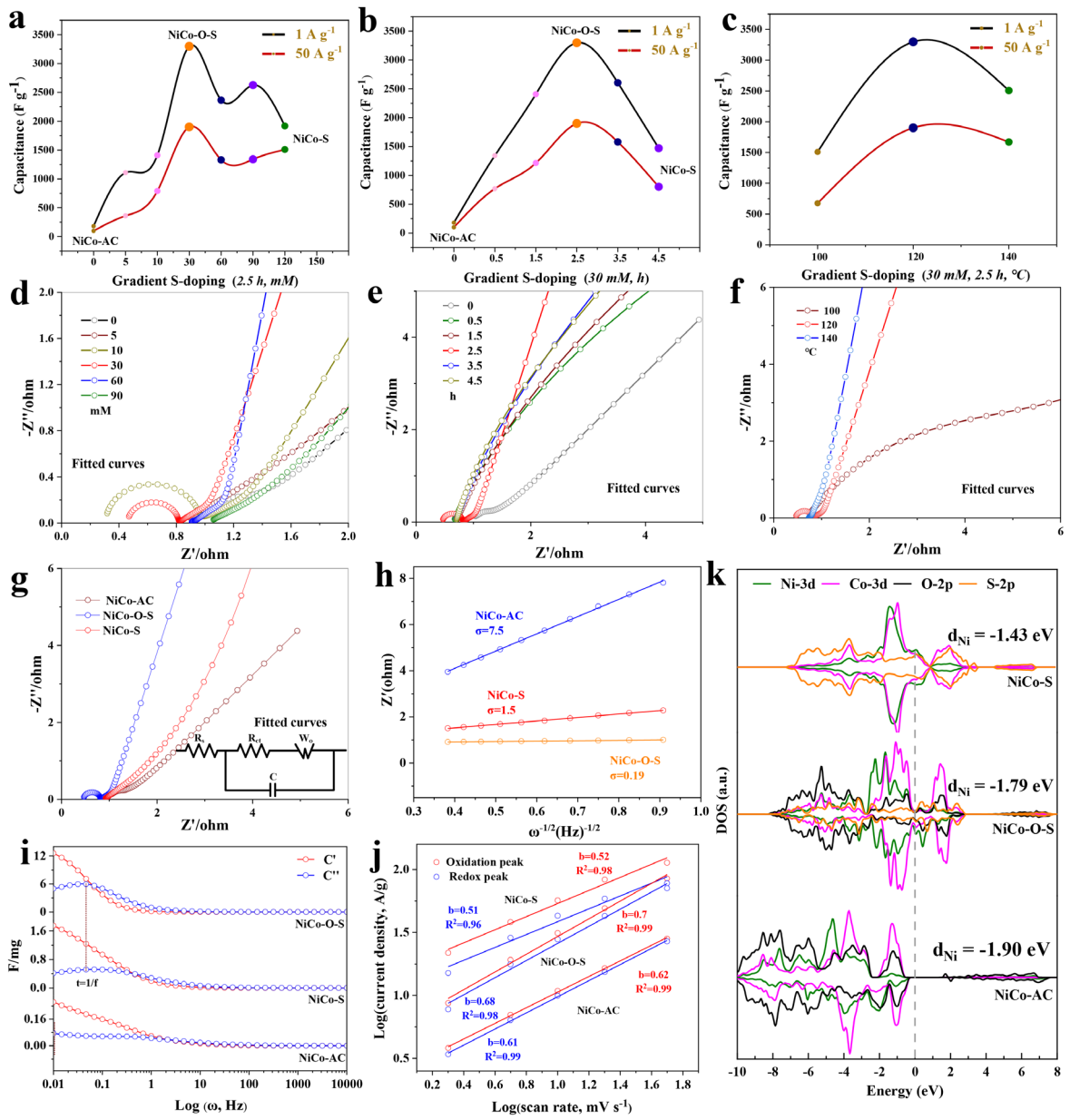

Figure 4. The gradient S-doping mass capacitance of NiCo-AC for a) with sodium sulfide of different concentrations and b) with different vulcanization time at the current densities of 1-50 A g^{-1}. c) Mass capacitance at different temperatures (100℃, 120℃ and 140℃) under the gradient S-doping conditions of 30mM and 2.5h. The gradient S-doping Nyquist curves with fitting data of NiCo-AC for d) concentration gradient and e) time gradient. f) Nyquist curves with fitting data at different temperatures (100℃, 120℃ and 140℃) under the gradient S-doping conditions of 30mM and 2.5h. g) The fitted Nyquist curves with equivalent circuit of NiCo-AC, NiCo-S and NiCo-O-S. h) The real part (Z′) vs. the reciprocal of the square root of frequency ($\omega^{-1/2}$) in intermediate frequency range to evaluate ion diffusion resistance, σ. i) Evolution of the real part $C'(\omega)$ and imaginary part $C''(\omega)$ capacitance *vs.* frequency. j) The peak currents against the scan rates of NiCo-AC, NiCo-O-S and NiCo-S. k) Density of states for NiCo-AC, NiCo-O and NiCo-O-S.

The Nyquist curves are measured in the frequency range of 0.01 to 100 kHz. Figures S11-13 reflect the Nyquist curves and their fitted curves for NiCo-O-S prepared with different gradient vulcanization conditions, as well as the Nyquist curves and their fitted curves for NiCo-AC and NiCo-S. As shown in **Figure 4**d-g, the fitted Nyquist curves are compared and analyzed. Obviously, the precisely regulated NiCo-O-S nanowires induced by fine gradient conditions exhibit the lowest solution internal resistance (R_s), interface charge transfer impedance (R_{ct}) and Warburg impedance (W_0), demonstrating that NiCo-O-S has higher electronic conductivity and lower ion diffusion resistance compared to NiCo-AC and NiCo-S (Table S2). Furthermore, the value of constant phase element (C) for NiCo-O-S is closer to 1 compared to NiCo-AC and NiCo-S, indicating that NiCo-O-S exhibits more ideal capacitive behavior. This is consistent with Figure S14a, showing that NiCo-O-S nanowire arrays reflect obviously enhanced charge storage capability based on the GCD curves. Significantly, as the current density increases by 50 times, the C_a can still reach 1900 F g^{-1}, reflecting a 58% capacitance retention rate (Figure S14b, c). To assess the ionic diffusion resistance (σ), the linear relationship between real part (Z′) and the reciprocal of the square root of frequency ($\omega^{-1/2}$) is described in the mid-frequency region. In **Figure 4**h, NiCo-O-S nanoarrays shows the minimum σ of 0.19 Ω $s^{-1/2}$ to indicate the most rapid OH^- permeation. As shown in **Figure4**i, the curvilinear relationship between capacitance $C'(\omega)$ and energy dissipation $C''(\omega)$ are depicted in low-frequency region from the following formulas (2-4), indicating that NiCo-O-S reflect the shortest dielectric relaxation time. Therefore, the novel core-shell structure induced by S doping can enhance electron transport efficiency and conductivity.

$$C(\omega) = C'(\omega) - jC''(\omega) \quad (2)$$

$$C'(\omega) = -Z''(\omega)/\omega|Z(\omega)|^2 \quad (3)$$

$$C'(\omega) = Z'(\omega)/\omega|Z(\omega)|^2 \quad (4)$$

Particularly, the linear correlation linking peak currents and the corresponding scan rates was described according to the formula (5) with constants *a* and *b*, and further analyzed the reaction kinetics of NiCo-O-S during the redox reaction process. The *b*-value reflect the energy storage type of electrode material [21, 22]. When 0.5<b<1.0, this indicates that the relationship between current and scan rate is partially linear, and the electrode material exhibits pseudocapacitive behavior. Significantly, the forms of charge transfer and storage can be divided into capacitive contribution (h_1v) and diffusion-controlled contribution ($h_2v^{1/2}$) based on the formula (6) with computational constants h_1 and h_2. In Figure 4j, the b-values of NiCo-O-S is 0.7, which is obviously higher than that of NiCo-S (0.51) and NiCo-AC (0.62), indicating that the replacement of some oxygen atoms with sulfur atoms leads to a significant increase in pseudo-capacitive contribution. With the increase in vulcanization intensity, the fully vulcanized NiCo-S exhibits characteristics of battery-type capacitance. In Figure S15a-c, the capacitance contribution rate of NiCo-O-S (61.1%) is obviously better than that of NiCo-AC (58.7%) and NiCo-S (42.3%) at 2 mV s^{-1}. As the scan rate is increased to 50 mV s^{-1}, the capacitance contribution of NiCo-O-S can reach as high as 90.2% (Figure S15d). Furthermore, at 5 and 50 mV s^{-1}, the capacitance contribution of NiCo-O-S is higher than that of NiCo-AC (67.4% and 87.8%) and NiCo-S (50.6% and 73.6%). Although NiCo-S exhibits higher capacitance performance than NiCo-AC, the b-value of NiCo-S is close to 0.5, indicating that the capacitance storage type of NiCo-S is diffusion-controlled battery-type and shows a lower pseudo-capacitance contribution compared to NiCo-AC. Therefore, sulfur doping can optimize the surface electronic states and enhance surface redox activity, effectively demonstrating that gradient S-doping NiCo-O-S has obviously enhanced pseudo-capacitive characteristics and a higher capacitance contribution compared to metal oxides and metal sulfides.

$$i = av^b \quad (5)$$

$$i = h_1 v + h_2 v^{1/2} \quad (6)$$

Generalized gradient approximation with Hubbard U correlation (GGA+U) is applied to analyze charge storage mechanism and characteristics of gradient sulfurization (U_{Ni}=4.5 and U_{Co}=3.52), and the calculation method is clearly described in the supporting information. As depicted in **Figure 4**k, the density of states (DOS) for NiCo-AC, NiCo-S and NiCo-O-S are compared and analyzed. The asymmetry in the spin-up and spin-down electrons in the d-bands of Ni and Co indicates that NiCo-AC (d_{Ni}=-1.90 eV), NiCo-S (d_{Ni}=-1.43 eV), and NiCo-O-S (d_{Ni}=-1.79 eV) exhibit magnetic properties. The absence of electron distribution near the Fermi level (0 eV) in NiCo-AC suggests its semiconductor nature, whereas the NiCo-S and NiCo-O-S gradually exhibit conductor properties, indicating that the gradient vulcanization effectively regulates electron transport efficiency and enhances conductivity. Especially, NiCo-AC has an obvious band gap near the Fermi level, while the band gaps of NiCo-S and NiCo-O-S are significantly reduced, allowing more electrons to enter the conduction band, which indicates that the introduction of S enhances the redox activity.

To investigate the impact of sulfur introduction on OH^{-1} adsorption sites, theoretical analysis was conducted on three different sites: Ni, Ni-Co, and Co. As shown in **Figure 5**a, OH^- can stably adsorb at the Ni sites of NiCo-AC and the adsorption energy ($E_{abs.}$) is -0.95 eV. When the adsorption site is Ni-Co, we observe that OH^- dissociates, and the hydrogen atom re-adsorbs onto the oxygen atom of NiCo-AC ($E_{abs.}$=-3.96 eV). When Co serves as the adsorption site, OH^- also undergoes significant dissociation and achieves stable adsorption at the Ni site ($E_{abs.}$=-4.75 eV). So, for NiCo-AC, the Ni site is the stable adsorption site for OH^-. In **Figure 5**b, as sulfur completely replaces oxygen, the OH^- adsorption sites change significantly in NiCo-S. The OH^- cannot stably adsorb at the Ni sites but instead adsorb at the S sites ($E_{abs.}$=-2.99 eV). When the adsorption sites are set to Ni-Co and Co, the

OH^- stably adsorb at the Ni-Ni sites ($E_{abs.}$=-2.75 eV), demonstrating that the Ni-Ni site is the reactive site during the redox process for NiCo-S. For NiCo-O-S (**Figure 5**c), OH^- can stably adsorb on the Ni site ($E_{abs.}$=-12.12 eV), but it dissociates at the Ni-Co site and adsorbs on the Ni-S site ($E_{abs.}$=-13.68 eV). As the active site is set to Co, the OH^- stably adsorbs on the Ni-Co-Ni site after calculation ($E_{abs.}$=-12.36 eV). Therefore, NiCo-O-S has a higher OH^- adsorption energy as compared to NiCo-AC and NiCo-S. After selecting the appropriate OH^- adsorption site, we further analyzed the charge density to reveal the mechanism of enhanced charge storage (yellow stands for electron-rich regions, while blue reflects electron-deficient regions, Isosurface level = 0.002). From the differential charge calculation results, it can be seen that the OH^- gains electrons from the surface of substrate, with electrons accumulating at the O end, while the substrate loses electrons. The area of the blue and yellow regions gradually increases in the order of NiCo-AC (**Figure 5**d), NiCo-S (**Figure 5**e), and NiCo-O-S (**Figure 5**f), indicating that the interaction between the OH^{-1} and the substrate becomes stronger. Overall, precise control of S doping can effectively regulate OH^- adsorption and charge storage capacity.

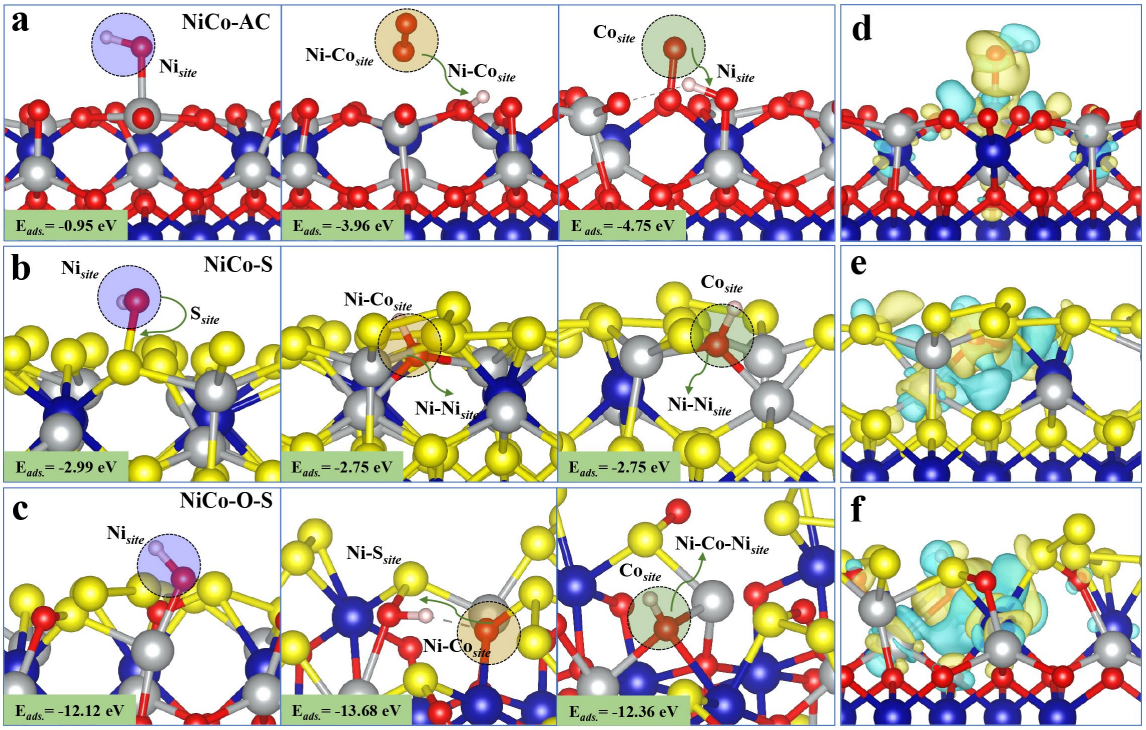

Figure 5. a-c) The geometry configuration of OH^- adsorption of NiCo-AC, NiCo-S and NiCo-O-S, with different active sites of Ni, Ni-Co, Co and their changes in adsorption process. d-f) The corresponding charge density of NiCo-AC, NiCo-S and NiCo-O-S for the reasonable adsorption sites.

Figure 6a illustrates the redox reaction process of the as-assembled hybrid supercapacitors (HSCs) device and its charge transfer and storage mechanism. The HSCs are assembled from NiCo-O-S (positive electrode) and active carbon (AC, negative electrode) in 3M potassium hydroxide (NiCo-O-S//AC). According to the positive and negative electrode charge matching rules (**Figure 6**b), including the voltage window of NiCo-O-S (0-0.5 V) and AC (−1-0 V), the two-electrode system is assembled to evaluate the performance of the HSCs. The C_a of negative electrode (Figure S16), the loading mass of AC, the calculation process, and the preparation of negative electrode are described in the supporting information. As shown in **Figure 6**c, a collection of CV curves originating from different voltage values is to determine the voltage window of HSCs is 1.7 v, because there is a clear polarization in the CV curve. Therefore, the steady voltage window is 0-1.6 V. As the scan rate gradually increases from 2 to 200 mV s^{-1}, it can be clearly observed that there is no significant change in these CV curves, proving an outstanding rate performance (**Figure 6**d). According to the GCD tests with a range of current densities between 1 and 20 A g^{-1}, C_a of the HSCs is 368 F g^{-1}. Especially, expanding the current density to 20 A g^{-1}, the HSCs can achieve a C_a of 221 F g^{-1}, demonstrating an ultra-high capacitance retention rate of 60%(**Figure 6e** and f).

Figure 6g presents the Ragone plot showing the relationship between energy density and power density. Specifically, the HSCs reflect the optimal energy density of 300 Wh kg^{-1} at the power density of 1,600 W kg^{-1}, and holds on 150 Wh kg^{-1} under the high-power density of 14,600 W kg^{-1}. Compared with reported similar supercapacitors in terms of energy density, our device exhibits obvious advantages, such as $NiCo_2S_4$//AC (69.6 Wh kg^{-1} at 847 W kg^{-1}) [23], Co_9S_8/NiCo-Mo//AC (37.6 Wh kg^{-}

^{1} at 228.7 W kg^{-1}) [24], Ag@NC//NWs-NCS (40 Wh kg^{-1} at 1100 W kg^{-1}) [25], NiCo-MOF-2//AC (45.7 Wh kg^{-1} at 450.6 W kg^{-1}) [26], NiCo-LDH@SiO_2/C//AC (47.6 Wh kg^{-1} at 1383 W kg^{-1}) [27], NiCo-LDH/(NiCo)Se_2@CC//AC (50.6 Wh kg^{-1} at 800 W kg^{-1}) [28], c-NiCo-LDH//AC(63.3 Wh kg^{-1} at 900 W kg^{-1}) [29], NiCo-P@CoNiMo-P//N-doped rGOs (81.4 Wh kg^{-1} at 1213 W kg^{-1}) [30], NiCo-LDH//MnO@NCN (94 Wh kg^{-1} at 1731.6 W kg^{-1}) [31], CF@NiCoZn-LDH/Co_9S_8-QD(56.4 Wh kg^{-1} at 875 W kg^{-1}) [32], $CoNi_2S_4$@NiCo-LDH/BC//AC(95.57 Wh kg^{-1} at 866.61 W kg^{-1}) [33]. Significantly, when current density is 20A g^{-1}, the C_a retention rate of the HSCs can reach up to 93.2% accompanied by a high coulombic efficiency of 98.5% after 12,000 charge-discharge cycles. Via comparing the first and the last 10 cycles based on the GCD curves, the NiCo-O-S//AC can be well matched with AC to assemble high-energy density supercapacitors, reflecting the enhanced electrochemical activity and stability at high current density with long charge-discharge (**Figure 6**h). Additionally, we characterized the nanowires after 12,000 cycles, showing that the bulk and crystal structure of NiCo-O-S exhibit outstanding stability (Figures S17, 18). To further analyze the evolution of the chemical composition during the redox reaction, we conducted in situ Raman testing of NiCo-O-S nanoarrays based on CV tests with different cycle numbers (1-18 cycles) at 5 m V s^{-1}. Owing to the NiCo-O-S nanowires are grown in situ on carbon fiber, the loading mass is relatively small, making it difficult to observe the characteristic peaks in-situ Raman characterization (FigureS19a, b). To address this issue, we prepared many nanoarrays electrode materials and ultrasonically transferred the active materials onto nickel foam (Figure S19c). During the CV cycling process, the in situ Raman characteristic peak positions of NiCo-O-S and H_2O molecules did not shift, but the intensity of the characteristic peaks increased obviously (Figure S19d). The unchanged characteristic peak positions indicates that the crystal structure of NiCo-O-S and the chemical environment in the electrochemical system remained

unchanged, further demonstrating the structural stability of the active material. Furthermore, the obvious increase in peak intensity suggests that the activity of NiCo-O-S enhances with the number of cycles, and the interaction between the hydroxyl groups (-OH) and NiCo-O-S strengthens. Therefore, NiCo-O-S can reflect high redox activity and reversibility.

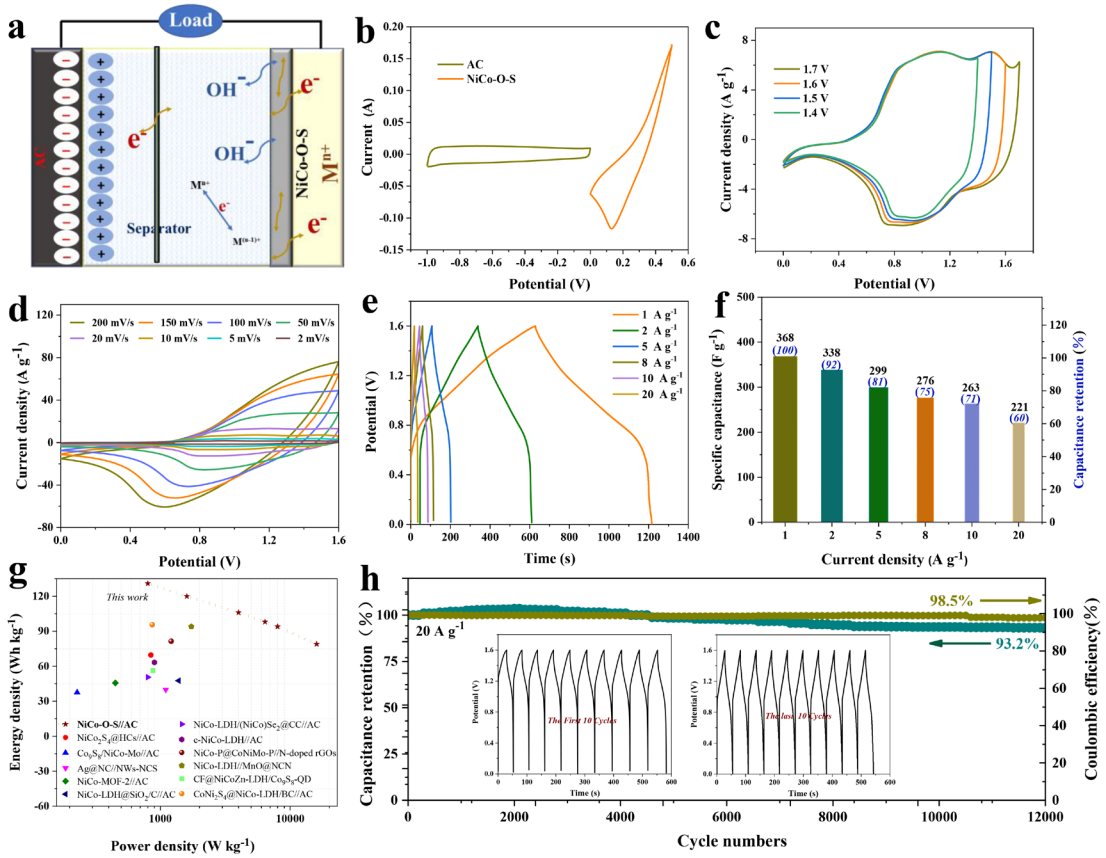

Figure 6. a) The principle of HSCs assembled by NiCo-O-S cathode and AC anode. b) CV curves of voltage matching for the NiCo-O-S and AC electrodes at 20 mV s^{-1}. c) CV curves used to determine the voltage window of HSCs. d) CV curves of the HSCs at different scan rates from 2 to 200 mV s^{-1}. e) GCD curves of the HSCs at different current densities from 1 to 20 A g^{-1}. f) The specific capacitance and retention rate of HSCs at different current density from 1 to 20 A g^{-1}. g) Ragone plots of the HSCs compared with the reported devices evaluated by mass energy density. h) Cycling performance of the HSCs for 12,000 cycles at 20 A g^{-1}, the inset reflects the charging-discharging GCD curves of the first and the last 10 cycles.

3. Conclusions

In order to enhance the bulk structure conductivity and electrochemical reaction activity of NiCo-AC,

the precise gradient sulfidation was proposed to in-situ construct NiCo-O-S core-shell structured nanowire arrays. Especially, the stable shell thickness is approximately 13 nm, and the core is composed of a large number of dispersed nanoparticles, which can enhance electrolyte adsorption and fully activate the active sites based on their synergistic effect. The S-induced intermediate state NiCo-O-S effectively regulated the surface and bulk structures of NiCo-AC, resulting in the reduction of band gap energy and the enhancement of reaction activity. Obviously, NiCo-O-S exhibits higher electrochemical energy storage efficiency as compared NiCo-AC and NiCo-S. Furthermore, using GGA+U theoretical calculations, the mechanisms toward the optimization of OH^- adsorption pathway and the surface charge density of NiCo-O-S were reasonably revealed. Therefore, the precise anion gradient regulation to ingeniously optimize the bulk structure and active center can provide a novel perspective and strategy for developing high-performance electrode materials.

Conflict of Interest

The authors declare no conflict of interest.

Acknowledgements

This work was supported by the Hong Kong Polytechnic University (Project No.: 1-W21C, 1-WZ1Y).

Reference

1. Yuan Y. J., Li X., Jiang L., Liang M., Zhang X. Q., Wu S. Y., Wu J. R., Tian M. Y., Zhao Y., Qu L. T. *Nat. Commun.*, **2023**, *14*(1): 3967.

2. Y. G. Yuan, L. Jiang, X. Li, P. Zuo, X. Q. Zhang, Y. L. Lian, Y. L. Ma, M. H. Liang, Y. Zhao, L. G. Qu, *Adv. Mater.* **2022**, *34,* 2110013.

3. Pameté E., Köps L., Kreth F. A., Pohlmann S., Varzi A., Brousse T., Balducci A., Presser V. *Adv. Energy Mater.,* **2023**, *13*(29): 2301008.

4. Y. L. Liu, C. Yan, G. G. Wang, F. Li, Q. Kang, H. Y. Zhang, J. C. Han, *Nanoscale*, 2020, 12(6): 4040-4050.

5. Zhang T., Matthews K., VahidMohammadi A., Han M., Gogotsi Y. *ACS Energy Lett.*, **2022**, *7*(11): 3864-3870.

6. Pham V. H., Wang C. J., Gao Y., Weidman J., Kim K., Matranga C. *Small Methods*, **2024**: 2301426.

7. Zhao Y. F., Ma H.N., Huang S. F., Zhang X. J., Xia M., Tang Y. F., Ma Z. F. *ACS appl. Mater. Inter.*, **2016**, *8*(35): 22997-23005.

8. Liu J.H., Li H. L., Cai J.Y., Liu J. Y., Liu Y. S., Sun Z. j., He X., Qu D. Z., Li X. *Chem. Front.*, **2022**, *9*(8): 1819-1829.

9. Zhu Z.N., Tian W., Lv X. B., Wang F. F., Hu Z. F., Ma K., Wang C. H., Yang T., Ji J.Y. *J. Colloid Interf. Sci.*, **2021**, *587*: 855-863.

10. Mao L., Zhao X., Li Y., Chen L. Y. *J. Colloid Interf. Sci.*, **2022**, *624*: 482-493.

11. Zhang Z.Y., Song N., Wang J., Liu Y. Q., Dai Z., Nie G.D. *SusMat*, **2022**, *2*(5): 646-657.

12. Zhao J. P., Wang Y. H., Qian Y. D., Jin H. L., Tang X. Y., Huang Z. M., Lou J. Y., Zhang Q. C., Lei Y., Wang S. *Adv. Funct. Mater.*, **2023**, *33*(4): 2210238.

13. Wang T., Wang Y., Lei J. Q., Chen K. J. Exploration. 2021, *1*(3): 20210178.

14. Pei L. J., Ji Y. H., Shi D., Yao J. N., Ren F. Y., Tan S. F., Lu F. X. *Mater. Let.*, **2022**, *325*: 132836.

15. Huang Y. J., Luo C., Zhang Q. B., Zhang H. H., Wang M. S. *J. Energy Chem.*, **2021**, *61*: 489-496.

16. Bandyopadhyay P., Saeed G., Kim N. H., Lee J. H. *Chem. Eng. J.*, **2020**, *384*: 123357.

17. Peng Z. Y., Huang Y. T., Bannov A. G., Li S. L., Tang L., Tan L. C., Chen Y. W. *Energy Environ. Sci.*, **2024**, *17*(10): 3384-3395.

18. Liu R. Q., Xu S. S., Shao X. X., Wen Y., Shi X. R., Huang L. P., Hong M., Hu J., Yang Z. *ACS Appl. Mater. Interfaces*, **2021**, *13*(40): 47717-47727.

19. Wang C., Song Z. H., Wan H. Z., Chen X., Tan Q. Y., Gan Y., Liang P., Zhang J., Wang H. B., Wang Y., Peng X. N., Aken P. A., Wang H. *Chem. Eng. J.*, **2020**, *400*: 125955.

20. Zhao J., Cheng H., Zhang Z. H., Liu Y., Song J. N., Liu T., He Y. N., Meng A. L., Sun C. L., Hu M. M., Wang L., Li G. C., Huang J. F., Li Z. J. *Adv. Funct. Mater.,* **2022**, *32*(33): 2202063.

21. Sikdar A., Héraly F., Zhang H., Hall K., Pang K. L., Zhang M., Yuan J. Y. *ACS nano*, **2024**, 18(4): 3707-3719.

22. Y. L. Liu, C. Yan, G. G. Wang, F. Li, Y. Shang, H. Y. Zhang, J. C. Han, H. Y. Yang, *Nanoscale*, 2020, 12(46): 23497-23505.

23. Zhao J. P., Wang Y. H., Qian Y. D., Jin H. L., Tang X. Y., Huang Z. M., Lou J. Y., Zhang Q. C., Lei Y., Wang S. *Adv. Funct. Mater.*, **2023,** *33*(4): 2210238.

24. Pan Y. F., Wei J. H., Han D. D., Xu Q., Gao D. Y., Yang Y. B., Wei Y. *Inorg. Chem. Front.*, **2021**, *8*(21): 4676-4684.

25. Zhong Y., Liang J. H., Zhang B. L., Wang F. M., Huang W. Q., Cai G. F., Zhang C., Lin Y., Chen B. H., He X. *Nanoscale*, **2022**, 14(22): 8172-8182.

26. Wang J. L., Liang J., Lin Y. C., Shao K. J., Chang X., Qian L. J., Li Z., Hu P. Z. *Chem. Eng. J.*, **2022**, *446*: 137368.

27. Yin B. Y., Hao L., Wei T., Chen W., Zhu B., Li X. G., Yang Q. G. *Chem. Eng. J.*, **2022**, *450*: 138224.

28. Jia H., Zhu X. Y., Song T. T., Pan J. P., Peng F., Li L. H., Liu Y. *J. Colloid Interf. Sci.*, **2022**, *608*: 175-185.

29. Liang Q. F., Jiang T. T., Zhang S. H., Long X. Y., Yan S. C., Dong R. T., Luo T. P., Xu X. T., Wang F. *J. Energy Storage*, **2021**, *41*: 102858.

30. Huang Y. J., Luo C., Zhang Q. B., Zhang H. H., Wang M. S. *J. Energy Chem.*, **2021**, *61*: 489-496.

31. Xing T., Sun M. Q., Guo S. Y., Harris O., Zhong Y. R., Tang L. Y., Zhang S. L., Yang M., Xia H. *J.*

Power Sources, **2021**, *495*: 229801.

32. Yang Q. J., Wang Q. S., Long Y., Wang F., Wu L. L., Pan J., Han J., Lei Y., Shi W. D., Song S. Y. *Adv. Energy Mater.*, **2020**, *10*(7): 1903193.

33. Wang H. Z., Gao X., Xie Y. Q., Guo E., Bai H., Jiang F., Li Q., Yue H. Y. *Adv. Energy Mater.*, **2024,** 2400493.